

Appearance of the Hoyle state and its breathing mode in ^{12}C despite strong short-range repulsion of the nucleon-nucleon potential

Hiroki Takemoto,^{1,2,*} Takayuki Myo,^{3,2} Hisashi Horiuchi,² Hiroshi Toki ,² Masahiro Isaka,⁴ Mengjiao Lyu,⁵ Qing Zhao ,⁶ and Niu Wan ⁷

¹Faculty of Pharmacy, Osaka Medical and Pharmaceutical University, Takatsuki, Osaka 569-1094, Japan

²Research Center for Nuclear Physics (RCNP), Osaka University, Ibaraki, Osaka 567-0047, Japan

³General Education, Faculty of Engineering, Osaka Institute of Technology, Osaka, Osaka 535-8585, Japan

⁴Science Research Center, Hosei University, Chiyoda-ku, Tokyo 102-8160, Japan

⁵College of Science, Nanjing University of Aeronautics and Astronautics, Nanjing 210016, China

⁶School of Science, Huzhou University, Huzhou 313000, Zhejiang, China

⁷School of Physics and Optoelectronics, South China University of Technology, Guangzhou 510641, China



(Received 16 December 2022; revised 27 February 2023; accepted 17 March 2023; published 5 April 2023)

In the ^{12}C nucleus, the Hoyle state (0_2^+) is considered to be an α -condensed state, and the 0_3^+ state is considered to be its breathing mode. We investigated whether the α condensation in ^{12}C is realized using a microscopic 3α cluster model with short-range correlation induced by nucleon-nucleon interactions, where we used the Argonne v_4' potential having a short-range repulsion constructed from the realistic Argonne v_{18} potential. Short-range correlation was treated using the unitary correlation operator method, and the Bloch–Brink wave function was adopted as a variational wave function where the α cluster motions were treated by generator coordinates. We obtained four 0^+ states, including short-range correlation, and analyzed them in terms of the Tohsaki–Horiuchi–Schuck–Röpke (THSR) wave function. In addition to the ordinary THSR wave function, we defined a second-order TSHR wave function to describe the $2\hbar\omega$ excitation of the α -condensed state. The 0_2^+ state (the Hoyle state) is an α -condensed state mainly comprising the $^8\text{Be}(0^+) + \alpha(0S\text{-wave})$ configuration, and the 0_3^+ state mainly comprises the $^8\text{Be}(0^+) + \alpha(2S\text{-wave})$ configuration, which is regarded as the breathing mode of the α condensation excited from the Hoyle state.

DOI: [10.1103/PhysRevC.107.044304](https://doi.org/10.1103/PhysRevC.107.044304)

I. INTRODUCTION

The nucleon-nucleon (NN) interaction provides the saturation property of the binding energy and density of the nuclear system, and it forms clusters as well as a mean field. According to the threshold rule (Ikeda’s diagram) [1], in self-conjugate $4n$ nuclei, one can expect the appearance of various cluster structures near the threshold energies that decay into relevant clusters [2]. A typical clustering state is the 0_2^+ state of ^{12}C located slightly above the 3α threshold energy, which is known as the Hoyle state and plays a crucial role in carbon synthesis in stars [3]. *Ab initio* calculations, e.g., the Green’s function Monte Carlo (GFMC) method [4,5], the lattice calculation of chiral effective-field theory (CEFT) [6], and no-core Monte Carlo shell model (MCSM) [7], indicated that the ground state of ^8Be and the Hoyle state has the α -cluster structure.

In the 1970s, one of the authors (H.H.) reported that the Hoyle state has a $^8\text{Be}(0_1^+) + \alpha(S\text{-wave})$ structure according to the orthogonality condition model (OCM) [8,9]. This indicates that the Hoyle state has a weakly coupled 3α structure because ^8Be has a well-developed 2α -cluster structure. This

gas-like α -clustering feature of the Hoyle state was confirmed by microscopic 3α cluster calculations [10–13]. In 2001, Tohsaki *et al.* proposed the concept of α condensation in finite nuclei by introducing the Tohsaki–Horiuchi–Schuck–Röpke (THSR) wave function [14] and confirmed that the Hoyle state is an α -condensed state in which constituent α clusters occupy the same $0s$ orbit. Subsequently, α condensation in finite nuclei was studied extensively from both experimental and theoretical perspectives [15].

For ^{12}C , several new states have been experimentally identified above the 3α threshold energy, such as 0_3^+ , 0_4^+ , 2_2^+ , and 4_2^+ states [16,17]; in particular, 0_3^+ and 0_4^+ states were recognized as a single state at an excitation energy of 10.3 MeV. The existence of 0_3^+ and 0_4^+ states was predicted by applying a complex-scaling method and analytic continuation of the coupling constant method to the 3α OCM [18]. The newly observed 0_3^+ state was identified as the breathing mode of the Hoyle state because of the high monopole strength between the 0_2^+ and 0_3^+ states estimated via the generator coordinate method (GCM) using the THSR wave function [19–21]. However, the 0_4^+ state has a bent-arm structure, as indicated by calculations using lattice CEFT [6], no-core MCSM [7], antisymmetrized molecular dynamics (AMD) [22], and fermionic molecular dynamics (FMD) [23]. Nevertheless, in previous theoretical research on α condensation in nuclei, the

*hiroki.takemoto@omp.u.ac.jp

phenomenological nuclear potential has been adopted as the NN interaction, similar to the Volkov force [24] without the short-range repulsion.

The objective of this study was to determine whether α -condensed states appear even if a NN potential has strong short-range repulsion as the first step in calculations using realistic NN interactions reproducing the experimental two-body data with high precision [25–27]. We use the Argonne v'_4 (AV4P) potential, which is a simplified potential prepared by projecting the Argonne v_{18} potential [25] to facilitate in many-body calculations [28]. The AV4P potential has a strong repulsive core which causes short-range correlations in nuclei. Therefore, we use the unitary correlation operator method (UCOM) [29] to treat the short-range correlations. In this method, correlations are included in the uncorrelated many-body wave function using a unitary transformation. Alternatively, a potential that includes the correlations is obtained by transforming the Hamiltonian. Therefore, it is possible to apply the UCOM procedure to variational many-body wave functions, such as FMD [30], the tensor-optimized shell model [31], and high-momentum AMD [32]. In this study, the Bloch–Brink (BB) wave function (the microscopic α -cluster model) [33] is adopted as an uncorrelated wave function, and the energy variation is performed by employing GCM calculations where the center-of-mass motions of α clusters are considered as generator coordinates. In addition, we determine whether the obtained low-lying 0^+ states are α -condensed states by evaluating the overlaps between their eigenfunctions and the THSR wave function. We further define the new THSR wave function describing the $2\hbar\omega$ excitation of the α -condensed state to analyze the GCM wave functions.

Section II A outlines the UCOM and provides preparation for the calculation using the AV4P potential. Section II B briefly explains the energy variation in the microscopic α -cluster model (the BB wave function). Section II C provides a brief explanation of the ordinal THSR wave function and defines the new THSR wave function to describe $2s$ and $2d$ excited states of α condensation. Section III presents the results for ^8Be and ^{12}C . In Section IV, the resultant 0^+ states are compared with other theoretical results and the overlaps with THSR wave functions are analyzed. In Sec. V, conclusions are presented, and future work is discussed.

II. METHODS AND PREPARATION

A. Unitary correlation operator method

The operator

$$\hat{C} = \exp\left(-i \sum_{i=1}^A \sum_{j=i+1}^A \hat{g}_{ij}\right) \quad (1)$$

is unitary when \hat{g}_{ij} is Hermitian (for simplicity, hereinafter, the subscript ij is omitted unless necessary). In the UCOM proposed by Feldmeier *et al.* [29] to treat short-range correlations, the Hermite operator \hat{g} is defined as follows:

$$\hat{g} = \frac{1}{2}\{\hat{p}_r s(r) + s(r)\hat{p}_r\}. \quad (2)$$

The operator \hat{p}_r is the component of the relative momentum \mathbf{p} parallel to the relative coordinate \mathbf{r} between the two nucleons, and $s(r)$ is the shift function. In the two-body case, the relative distance r and operator \hat{p}_r are transformed as follows:

$$\hat{c}^\dagger r \hat{c} = R_+(r), \quad \hat{c}^\dagger \hat{p}_r \hat{c} = \sqrt{\frac{1}{R'_+(r)}} \hat{p}_r \sqrt{\frac{1}{R'_+(r)}}. \quad (3)$$

Here, $\hat{c} = \exp(-i\hat{g})$, and the correlation function $R_+(r)$ is related to the shift function $s(r)$ as follows:

$$\frac{dR_+(r)}{dr} = \frac{s(R_+(r))}{s(r)}. \quad (4)$$

The expectation value of the Hamiltonian with respect to the correlated A -body wave function $|\tilde{\Psi}\rangle (= \hat{C}|\Psi\rangle)$ is given by

$$E = \frac{\langle \tilde{\Psi} | \hat{H} | \tilde{\Psi} \rangle}{\langle \tilde{\Psi} | \tilde{\Psi} \rangle} = \frac{\langle \Psi | \hat{C}^\dagger \hat{H} \hat{C} | \Psi \rangle}{\langle \Psi | \hat{C}^\dagger \hat{C} | \Psi \rangle} = \frac{\langle \Psi | \tilde{H} | \Psi \rangle}{\langle \Psi | \Psi \rangle}. \quad (5)$$

The transformed Hamiltonian \tilde{H} is defined as follows:

$$\tilde{H} = \hat{C}^\dagger \hat{T} \hat{C} + \hat{C}^\dagger \hat{V} \hat{C} = \tilde{T} + \tilde{V}. \quad (6)$$

In the two-body approximation, which is valid in the short-range case, the transformed two-body potential is given as follows:

$$\tilde{V} \simeq \sum_{i=1}^A \sum_{j=i+1}^A v(R_+(r_{ij})), \quad (7)$$

and the transformed kinetic energy consists of the uncorrelated term \tilde{T} and correlated two-body term \tilde{T}_2 :

$$\tilde{T} \simeq \hat{T} + \tilde{T}_2. \quad (8)$$

The kinetic energy of the center-of-mass motion of the total system is subtracted from the uncorrelated term as follows:

$$\hat{T} = \sum_{i=1}^A \hat{t}_i - \hat{T}_{\text{c.m.}}, \quad (9)$$

and the correlated two-body term depends on the momentum and angular momentum of relative motion:

$$\tilde{T}_2 = \sum_{i=1}^A \sum_{j=i+1}^A (w_{ij} + u_{ij}^p + u_{ij}^l), \quad (10)$$

where

$$w = \frac{\hbar^2}{m} \left(\frac{7 R_+''(r)}{4 R_+^4(r)} - \frac{1 R_+''(r)}{2 R_+^3(r)} \right),$$

$$u^p = \frac{1}{2m} \left\{ \hat{p}^2 \left(\frac{1}{R_+^2(r)} - 1 \right) + \left(\frac{1}{R_+^2(r)} - 1 \right) \hat{p}^2 \right\},$$

$$u^l = \frac{1}{m} \left(\frac{r^2}{R_+^2(r)} - \frac{1}{R_+^2(r)} \right) l^2.$$

In the procedure proposed in Ref. [29], the correlation function $R_+(r)$ is assumed to have a specific form. In this study, we employed a form similar to that used in Ref. [34] for odd and even channels:

$$R_+^{\text{even}}(r) = r + \alpha(r/\beta)^\eta \exp(-e^{r/\beta}) \quad (11)$$

TABLE I. Parameters of the correlation functions $R_+(r)$ for the AV4P potential determined in Ref. [35].

	α [fm]	β [fm]	γ [fm]	η
1E	1.36	0.98		0.33
3E	1.24	0.94		0.39
1O	1.50	1.26	0.87	
3O	0.69	1.39	0.28	

and

$$R_+^{\text{odd}}(r) = r + \alpha(1 - e^{-r/\gamma}) \exp(-e^{r/\beta}), \quad (12)$$

respectively. In principle, although α , β , γ , and η are variational parameters, common values (Table I) were used in this study for calculating ^4He , ^8Be , and ^{12}C nuclei, which were determined in Ref. [35] to minimize the energy of symmetric nuclear matter at a saturation density of 0.17 fm^{-3} using the AV4P potential.

Figure 1 shows the AV4P potential (circles) and the potential transformed by the UCOM procedure (squares) with respect to the distance between two nucleons in each channel. Reflecting the difference in correlation functions of even and odd channels, the region of the repulsive core was largely reduced in even channels by the UCOM, whereas the

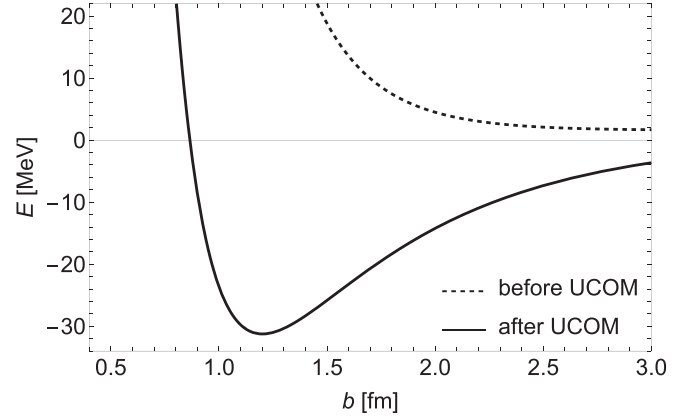


FIG. 2. Energy curves of ^4He with the $(0s)^4$ configuration using the AV4' potential as a function of the size parameter b . The dashed and solid curves are the energy curves before and after the translation via the UCOM, respectively.

reduction was relatively small in odd channels. For numerical calculations, the transformed potentials were fit by the sum of 15 Gaussians (solid curves), and the Coulomb potential was similarly included. Figure 2 shows the effect of the UCOM

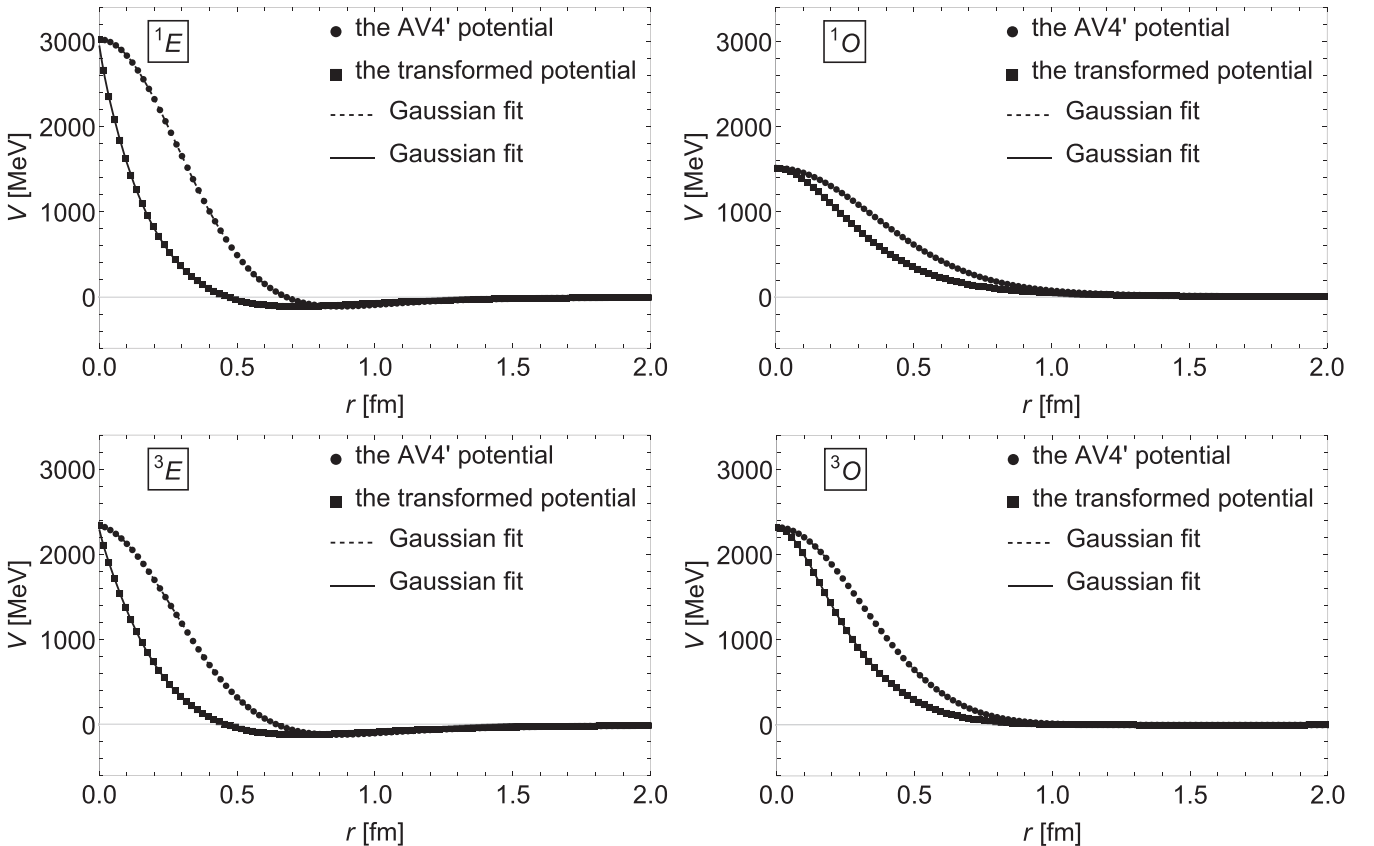


FIG. 1. Original AV4P potential (circles) and the transformed one (squares) obtained via the UCOM in the 1E (upper-left panel), 3E (lower-left panel), 1O (upper-right panel), and 3O (lower-right panel) channels. The dashed and the solid curves are the fitting curves based on the sum of 15 Gaussians for the original and transformed potentials, respectively.

TABLE II. Comparison of the energy and root-mean-square radius of ${}^4\text{He}$ at the minimum-energy point with values from the GFMC method and experimental data. The experimental value of the charge radius was converted into the point-proton radius.

	E [MeV]	$\sqrt{\langle r^2 \rangle}$ [fm]
UCOM [(0s) ⁴]	-31.24	1.29
GFMC	-32.11(2)	
EXPR	-28.3	1.46

on the energy of ${}^4\text{He}$ with the (0s)⁴ configuration:

$$\psi_0(\alpha) = \mathcal{A} \prod_{i=1}^4 \phi_0(\mathbf{r}_i) \chi_i(\xi_i), \quad (13)$$

where $\chi_1, \chi_2, \chi_3, \chi_4 = p_\uparrow, p_\downarrow, n_\uparrow, n_\downarrow$, and

$$\phi_{\mathbf{R}}(\mathbf{r}) = \left(\frac{1}{\sqrt{\pi}b} \right)^{3/2} \exp \left[-\frac{1}{2b^2} (\mathbf{r} - \mathbf{R})^2 \right]. \quad (14)$$

Excluding short-range correlations (dashed curve), the four-nucleon system is unbound, but in cases with short-range correlations included via the UCOM (solid curve), the ${}^4\text{He}$ nucleus becomes bound. In Table II, the energy and root-mean-square radius of ${}^4\text{He}$ at the minimum-energy point are compared with the results of the GFMC method and experimental data. The UCOM calculation almost reproduced the GFMC calculation, and the energy difference is approximately 0.9 MeV. Both the UCOM and GFMC calculations yield lower energies than the experimental data, and the size of the α particle is significantly smaller than the observed value, which is due to the nature of the AV4P potential without the tensor force.

B. Variational wave function

The BB wave function was proposed to describe an α -cluster state of self-conjugate $4n$ -nuclei [33] and is expressed as

$$\langle \mathbf{r} | \Phi_{\text{BB}}(\Gamma) \rangle = \mathcal{A} \prod_{i=1}^n \psi_{\mathbf{R}_i}(\alpha_i), \quad (15)$$

where Γ denotes the set of n vectors $\{\mathbf{R}_1, \mathbf{R}_2, \dots, \mathbf{R}_n\}$ specifying the positions of α clusters. When the size parameter of cluster b is common to all the constituent clusters, the BB wave function can be separated into the center-of-mass and relative parts:

$$\langle \mathbf{r} | \Phi_{\text{BB}}(\Gamma) \rangle = \langle \mathbf{r}_{\text{c.m.}} | \Phi_{\text{BB}}^{\text{c.m.}}(\mathbf{R}_{\text{c.m.}}) \rangle \langle \tilde{\mathbf{r}} | \Phi_{\text{BB}}^{\text{rel}}(\tilde{\Gamma}) \rangle, \quad (16)$$

where $\mathbf{r}_{\text{c.m.}}$ and $\tilde{\mathbf{r}}$ are the center-of-mass and Jacobi's coordinates, respectively. The vector $\mathbf{R}_{\text{c.m.}}$ represents the mean position of the clusters.

$$\mathbf{R}_{\text{c.m.}} = \frac{1}{n} \sum_{i=1}^n \mathbf{R}_i, \quad (17)$$

and $\tilde{\Gamma}$ represents a set of $n-1$ vectors $\{\tilde{\mathbf{R}}_1, \dots, \tilde{\mathbf{R}}_{n-1}\}$, which are written as

$$\tilde{\mathbf{R}}_k = \mathbf{R}_{k+1} - \frac{1}{k} \sum_{i=1}^k \mathbf{R}_i \quad (18)$$

for $k = 1, 2, \dots, n-1$. The eigenstate of the total angular momentum is expressed as

$$\langle \mathbf{r} | \Phi_{MK}^J(\Gamma) \rangle = \langle \mathbf{r} | \hat{P}_{MK}^J | \Phi_{\text{BB}}(\Gamma) \rangle \quad (19)$$

and

$$\hat{P}_{MK}^J = \frac{2J+1}{8\pi^2} \int d\psi D_{MK}^J(\psi) \hat{\mathcal{R}}(\psi), \quad (20)$$

where $\hat{\mathcal{R}}(\psi)$ and $D_{MK}^J(\psi)$ are unitary operators that rotate a wave function by Euler angles ψ and a unitary rotation matrix, respectively. In the calculations, the mean position of the clusters in Eq. (17) is considered the origin, and the integration of Euler angles is numerically performed using the Gauss-Legendre quadrature.

A better wave function can be obtained by taking a linear combination of the wave functions [Eq. (19)] for different configurations Γ :

$$\langle \mathbf{r} | \Psi_{MK}^J \rangle = \int d\Gamma c(\Gamma) \langle \mathbf{r} | \Phi_{MK}^J(\Gamma) \rangle. \quad (21)$$

The center-of-mass and relative wave functions are separable, provided that

$$c(\Gamma) = c_{\text{c.m.}}(\mathbf{R}_{\text{c.m.}}) c_{\text{rel}}(\tilde{\Gamma}). \quad (22)$$

The coefficients $c(\Gamma)$ are determined by the variational principle for the total energy E :

$$\delta (\langle \Psi_{MK}^J | \hat{H} | \Psi_{MK}^J \rangle / \langle \Psi_{MK}^J | \Psi_{MK}^J \rangle) = 0, \quad (23)$$

where K mixing is not taken into account, and Eq. (23) leads to the Hill-Wheeler equation. Instead of using the integral combination in Eq. (21), we use a linear combination with a finite number:

$$\langle \mathbf{r} | \Psi_{MK}^J \rangle = \sum_{i=1}^N c(\Gamma_i) \langle \mathbf{r} | \Phi_{MK}^J(\Gamma_i) \rangle. \quad (24)$$

Then, solving the Hill-Wheeler equation becomes an eigenvalue problem for coefficients $c(\Gamma_i)$:

$$\sum_{i=1}^N (\mathcal{H}_{ij} - E \mathcal{N}_{ij}) c(\Gamma_j) = 0, \quad (25)$$

where

$$\mathcal{H}_{ij} = \langle \Phi_{MK}^J(\Gamma_i) | \hat{H} | \Phi_{MK}^J(\Gamma_j) \rangle \quad (26)$$

and

$$\mathcal{N}_{ij} = \langle \Phi_{MK}^J(\Gamma_i) | \Phi_{MK}^J(\Gamma_j) \rangle. \quad (27)$$

The eigenvalue problem is solved under the condition that $\mathbf{R}_{\text{c.m.}}$ is fixed at the origin; that is, $c_{\text{c.m.}}(\mathbf{R}_{\text{c.m.}}) = \delta(\mathbf{R}_{\text{c.m.}})$, which satisfies Eq. (22).

C. Tohsaki-Horiuchi-Schuck-Röpke wave function

To determine whether the obtained 0^+ states in GCM calculations are α -condensed states, we evaluated the overlaps between their eigenfunctions and the THSR wave function. The THSR wave function was proposed to describe the $n\alpha$ condensed states [15] and is a linear combination of the BB wave functions assuming that the weight function follows a normal distribution (hereinafter, the original spherical THSR wave function is called the $0s$ -THSR wave function):

$$\langle \mathbf{r} | \Psi_{\text{THSR}}^{(0s)}(B) \rangle = \int d\Gamma N_B^{(0)}(\Gamma) \langle \mathbf{r} | \Phi_{\text{BB}}(\Gamma) \rangle, \quad (28)$$

where

$$N_B^{(0)}(\Gamma) = \prod_{i=1}^n \exp\left(-\frac{\mathbf{R}_i^2}{2B^2}\right). \quad (29)$$

To describe the $2\hbar\omega$ excitation of the α -condensed states, wherein one α particle is excited to the $2s$ or $2d$ orbit in a dilute system, we first introduced the second-order THSR wave function as follows:

$$\langle \mathbf{r} | \Psi_{\text{THSR}}^{(2)}(B) \rangle = \int d\Gamma N_B^{(2)}(\Gamma) \langle \mathbf{r} | \Phi_{\text{BB}}(\Gamma) \rangle, \quad (30)$$

where

$$N_B^{(2)}(\Gamma) = \sum_{i=1}^n \frac{\mathbf{R}_i^2}{B^2} N_B^{(0)}(\Gamma). \quad (31)$$

The $2s$ -THSR wave function is constructed by imposing the orthogonality to the $0s$ -THSR wave function with the same parameter B :

$$\begin{aligned} \langle \mathbf{r} | \Psi_{\text{THSR}}^{(2s)}(B) \rangle &= \langle \mathbf{r} | \Psi_{\text{THSR}}^{(2)}(B) \rangle \\ &\quad - \frac{\langle \Psi_{\text{THSR}}^{(0s)}(B) | \Psi_{\text{THSR}}^{(2)}(B) \rangle}{\langle \Psi_{\text{THSR}}^{(0s)}(B) | \Psi_{\text{THSR}}^{(0s)}(B) \rangle} \langle \mathbf{r} | \Psi_{\text{THSR}}^{(0s)}(B) \rangle, \end{aligned} \quad (32)$$

and the $2d$ -THSR wave function is constructed by multiplying Eq. (31) by the spherical harmonics $Y_2^m(\theta, \phi)$:

$$\langle \mathbf{r} | \Psi_{\text{THSR}}^{(2d_m)}(B) \rangle = \int d\Gamma Y_2^m(\theta, \phi) N_B^{(2)}(\Gamma) \langle \mathbf{r} | \Phi_{\text{BB}}(\Gamma) \rangle. \quad (33)$$

By integrating over configuration Γ within the dilute limit that B is sufficiently large to neglect antisymmetrization, we can verify that the $0s$ -THSR wave function represents the α -condensed state in which all α particles occupy the same $0s$ orbit and that the $2s$ - or $2d$ -THSR wave function represents the α -condensed state in which one of the α clusters is excited to the $2s$ or $2d$ orbit:

$$\langle \mathbf{r} | \Psi_{\text{THSR}}^{(0s)}(B) \rangle \propto \prod_{i=1}^n \exp\left(-\frac{\mathbf{X}_i^2}{2B_c^2}\right) \varphi(\alpha_i), \quad (34)$$

$$\langle \mathbf{r} | \Psi_{\text{THSR}}^{(2s)}(B) \rangle \propto \sum_{k=1}^n \left(1 - \frac{2}{3} \frac{\mathbf{X}_k^2}{B_c^2}\right) \prod_{i=1}^n \exp\left(-\frac{\mathbf{X}_i^2}{2B_c^2}\right) \varphi(\alpha_i), \quad (35)$$

and

$$\langle \mathbf{r} | \Psi_{\text{THSR}}^{(2d_m)}(B) \rangle \propto \sum_{k=1}^n Y_2^m(\theta, \phi) \frac{\mathbf{X}_k^2}{B_c^2} \prod_{i=1}^n \exp\left(-\frac{\mathbf{X}_i^2}{2B_c^2}\right) \varphi(\alpha_i), \quad (36)$$

where \mathbf{X}_i and $\varphi(\alpha_i)$ are the center-of-mass coordinate and internal wave function of the i th α cluster, respectively, and $B_c = B[1 + (b/2B)^2]^{1/2}$.

The $0s$ -, $2s$ - and $2d$ -THSR wave function can be separated into the center of mass and relative parts because the weight functions $N_B^{(0)}(\Gamma)$ and $N_B^{(2)}(\Gamma)$ satisfy the condition of Eq. (22). Accordingly, the wave function of all the relative motions with $0s$ -wave (capital letters mean the relative motion) is given by

$$\langle \tilde{\mathbf{r}} | \Psi_{\text{rel}}^{(0s)}(\tilde{B}) \rangle = \int d\tilde{\Gamma} \tilde{N}_{\tilde{B}}^{(0)}(\tilde{\Gamma}) \langle \tilde{\mathbf{r}} | \Phi_{\text{BB}}^{\text{rel}}(\tilde{\Gamma}) \rangle, \quad (37)$$

and the wave function wherein one of relative motions is $2S$ wave or $2D$ wave is given by

$$\begin{aligned} \langle \tilde{\mathbf{r}} | \Psi_{\text{rel}}^{(2S)}(\tilde{B}) \rangle_{\tilde{R}_i} &= \langle \tilde{\mathbf{r}} | \Psi_{\text{rel}}^{(2)}(\tilde{B}) \rangle_{\tilde{R}_i} \\ &\quad - \frac{\langle \Psi_{\text{rel}}^{(0s)}(\tilde{B}) | \Psi_{\text{rel}}^{(2)}(\tilde{B}) \rangle_{\tilde{R}_i}}{\langle \Psi_{\text{rel}}^{(0s)}(\tilde{B}) | \Psi_{\text{rel}}^{(0s)}(\tilde{B}) \rangle} \langle \tilde{\mathbf{r}} | \Psi_{\text{rel}}^{(0s)}(\tilde{B}) \rangle, \end{aligned} \quad (38)$$

where

$$\langle \tilde{\mathbf{r}} | \Psi_{\text{rel}}^{(2)}(\tilde{B}) \rangle_{\tilde{R}_i} = \int d\tilde{\Gamma} \frac{\tilde{\mathbf{R}}_i^2}{\tilde{B}^2} N_{\tilde{B}}^{(0)}(\tilde{\Gamma}) \langle \tilde{\mathbf{r}} | \Phi_{\text{BB}}(\tilde{\Gamma}) \rangle, \quad (39)$$

or

$$\langle \tilde{\mathbf{r}} | \Psi_{\text{rel}}^{(2D_m)}(\tilde{B}) \rangle_{\tilde{R}_i} = \int d\tilde{\Gamma} Y_2^m(\theta, \phi) \frac{\tilde{\mathbf{R}}_i^2}{\tilde{B}^2} N_{\tilde{B}}^{(0)}(\tilde{\Gamma}) \langle \tilde{\mathbf{r}} | \Phi_{\text{BB}}(\tilde{\Gamma}) \rangle. \quad (40)$$

Here, the weight function is given by

$$N_{\tilde{B}}^{(0)}(\tilde{\Gamma}) = \prod_{i=1}^{n-1} \exp\left(-\frac{\tilde{\mathbf{R}}_i^2}{2\tilde{B}_i^2}\right), \quad (41)$$

with

$$\tilde{B}_k = \sqrt{\frac{k+1}{k}} B \quad (42)$$

for $k = 1, 2, \dots, n-1$, and \tilde{B} denotes the parameter set of $\{\tilde{B}_1, \dots, \tilde{B}_{n-1}\}$. In the following calculations, the parameters $\tilde{B}_1, \tilde{B}_2, \dots$, and \tilde{B}_{n-1} are assumed to be independent,

$$\tilde{B}_k = \sqrt{\frac{k+1}{k}} B_k, \quad (43)$$

to include the ${}^8\text{Be} + \alpha$ channel in the 3α system, which is called the extended THSR wave function [36].

III. RESULTS

A. ${}^8\text{Be}$

The GCM calculation was performed for 0^+ states of ${}^8\text{Be}$ whose wave function is expressed as follows:

$$\langle \tilde{\mathbf{r}} | \Phi_{2\alpha}(0^+) \rangle = \langle \tilde{\mathbf{r}} | \hat{P}_{00}^0 | \Phi_{\text{BB}}(\tilde{\mathbf{R}}) \rangle, \quad (44)$$

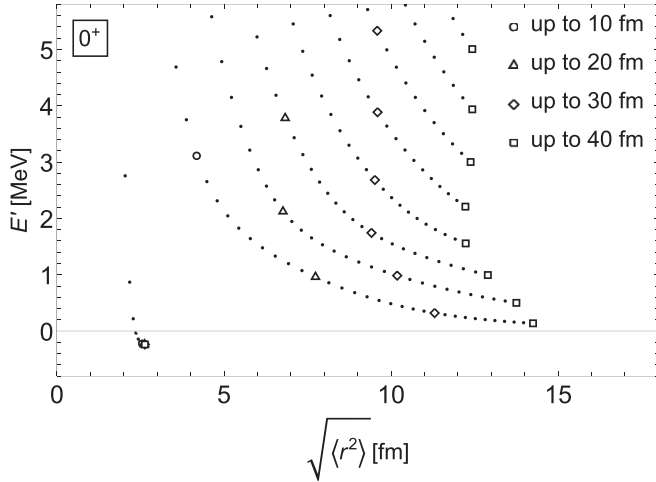


FIG. 3. Trajectories of the eigenstates of ${}^8\text{Be}(0^+)$ in the $(\langle r^2 \rangle)^{1/2}$ (root-mean-square radii of eigenstates) and E' (eigenvalues measured from the threshold energy of the 2α breakup, $E' = E - 2E_\alpha$) plane as the number of generator coordinates increases from 1 fm at 1-fm intervals. Circles, triangles, diamonds, and squares indicate the calculations up to 10, 20, 30, and 40 fm, respectively.

where $\tilde{\mathbf{R}} = \mathbf{R}_2 - \mathbf{R}_1 = (0, 0, R)$. The size parameter b was set as 1.20 fm, corresponding to the free α particle. The generator coordinate R was chosen from 1 fm at 1-fm intervals. Figure 3 shows the trajectories of the eigenstates in the $(\langle r^2 \rangle)^{1/2}$ (root-mean-square radii of eigenstates) and E' (eigenvalues measured from the threshold energy of the 2α breakup, $E' = E - 2E_\alpha$) plane as the number of generator coordinates increases from 1 fm at 1-fm intervals. Clearly, only the lowest eigenstate had the converged values for $(\langle r^2 \rangle)^{1/2}$ and E' . In Table III, the energy and root-mean-square radius of the ground state of ${}^8\text{Be}$ are compared with the GFMC results and the experimental data. The AV4P potential bounded ${}^8\text{Be}$ in both the present and GFMC calculations, although the ${}^8\text{Be}$ nucleus was observed as a resonance. The energy difference between the present and GCM calculations was approximately 0.55 MeV when the energy was measured from the threshold energy for decay into 2α particles. From its radius, the density of ${}^8\text{Be}$ was estimated to be 0.236 times that of ${}^4\text{He}$, indicating that the ground state of ${}^8\text{Be}$ is diluted.

Figure 4 presents the squared overlaps between the $0S$ -THSR and eigenfunctions obtained from the GCM calculations up to 40 fm. In the UCOM procedure, the overlap

TABLE III. Comparison of the energy and the root-mean-square radius of the ground state of ${}^8\text{Be}$ obtained from the GCM calculation with values from the GFMC method and experimental data. E' was measured from the threshold energy for decay into 2α particles ($E' = E - 2E_\alpha$).

	E [MeV]	E' [MeV]	$\sqrt{\langle r^2 \rangle}$ [fm]
BB + GCM	-62.71	-0.23	2.63
GFMC	-65.0(1)	-0.78(14)	
EXPR	-56.5	0.11	

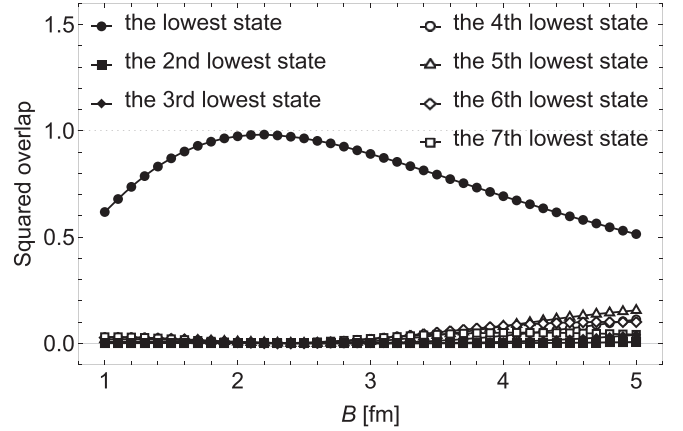


FIG. 4. Squared overlaps between the $0S$ -THSR wave function and eigenfunctions from the lowest eigenstate to the seventh-lowest eigenstate of ${}^8\text{Be}(0^+)$ obtained via the GCM calculation up to 40 fm.

between two correlated wave functions is equivalent to that between two uncorrelated wave functions: $\langle \tilde{\Phi} | \tilde{\Psi} \rangle = \langle \Phi | U^\dagger U | \Psi \rangle = \langle \Phi | \Psi \rangle$. The maximum value of the squared overlap of the lowest state was 0.982 at $B = 2.2$ fm. Therefore, the ground state of ${}^8\text{Be}$ obtained in the present calculations is considered to be an α -condensed state, where α particles occupy the same $0s$ orbit, because it is diluted and can be described by a single $0S$ -THSR wave function.

B. ${}^{12}\text{C}$

The wave functions of ${}^{12}\text{C}(0^+)$ were constructed by projecting the α - $2\alpha(0^+)$ systems to 0^+ states (the double angular-momentum projection), as shown in Fig. 5:

$$\langle \tilde{r} | \Phi_{3\alpha}(0^+) \rangle = \langle \tilde{r} | \hat{P}_{00}^0 | \mathcal{A}[\Phi_\alpha \Phi_{2\alpha}(0^+)] \rangle. \quad (45)$$

The GCM calculations for $\tilde{\mathbf{R}}_1$ and $\tilde{\mathbf{R}}_2$ were performed from 1 fm at 1-fm intervals.

By checking the trajectories of eigenstates in the $(\langle r^2 \rangle)^{1/2}$ and E' ($=E - 3E_\alpha$) plane and strengths of the monopole

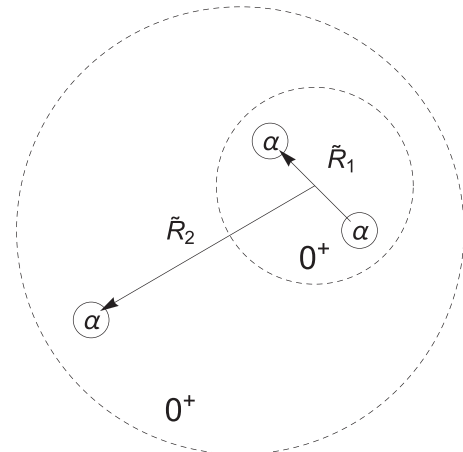


FIG. 5. Configuration of three α clusters in ${}^{12}\text{C}$ adopted for the GCM calculation, where two α system is projected to the 0^+ state.

TABLE IV. Energies, root-mean-square radii, and matrix elements of the monopole transition of the nine lowest eigenstates of ^{12}C obtained via the GCM calculation up to $(\tilde{R}_1, \tilde{R}_2) = (16 \text{ fm}, 16 \text{ fm})$. The units for the energies, root-mean-square radii, and matrix elements of the monopole transition are MeV, fm, and $e \text{ fm}^2$, respectively.

Eigenstate	E	$\sqrt{\langle r^2 \rangle}$	Monopole transition matrix element	
			$0^+ \rightarrow 0_1^+$	$0^+ \rightarrow 0_2^+$
1st (0_1^+)	-102.32	2.18		5.37
2nd (0_2^+)	-93.12	3.50	5.37	
3rd (0_3^+)	-91.90	6.41	1.61	33.60
4th	-90.53	7.45	1.38	9.84
5th	-90.26	6.50	1.65	13.23
6th	-88.86	6.83	1.25	1.59
7th	-88.56	7.18	0.65	3.39
8th (0_4^+)	-88.03	5.15	3.03	3.92
9th	-87.94	5.88	0.35	7.52

transition, four 0^+ states were identified, which are shown in parentheses in Table IV. Figure 6 shows the distribution of eigenstates in the $(\langle r^2 \rangle)^{1/2}$ - E' plane, where dots are added for every additional generator coordinate, and green circles, blue triangles, and red diamonds indicate the calculations up to $(\tilde{R}_1, \tilde{R}_2) = (10 \text{ fm}, 10 \text{ fm})$, $(13 \text{ fm}, 13 \text{ fm})$, and $(16 \text{ fm}, 16 \text{ fm})$, respectively. Table IV presents the energies, root-mean-square radii, and matrix elements of the monopole transition of the nine lowest eigenstates of ^{12}C obtained via the GCM calculation up to $(\tilde{R}_1, \tilde{R}_2) = (16 \text{ fm}, 16 \text{ fm})$.

For the ground state (0_1^+) and Hoyle state (0_2^+), both the energy and root-mean-square radius converged (trajectories I and II in Fig. 6). The Hoyle state was obtained as a resonant state but had a finite radius owing to the Coulomb barrier.

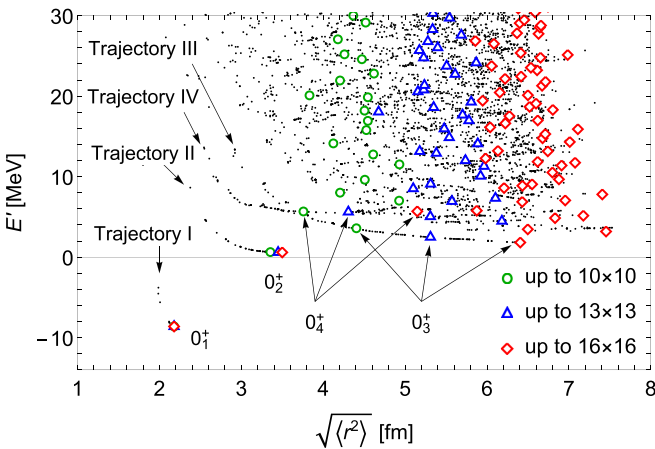


FIG. 6. Trajectories of the eigenstates of $^{12}\text{C}(0^+)$ in the $(\langle r^2 \rangle)^{1/2}$ - E' ($=E - 3E_\alpha$) plane. Green circles, blue triangles, and red diamonds indicate the calculations up to $(\tilde{R}_1, \tilde{R}_2) = (10 \text{ fm}, 10 \text{ fm})$, $(13 \text{ fm}, 13 \text{ fm})$, and $(16 \text{ fm}, 16 \text{ fm})$, respectively, from $(\tilde{R}_1, \tilde{R}_2) = (1 \text{ fm}, 1 \text{ fm})$ at 1-fm intervals for each generator coordinate.

For the 0_4^+ state (trajectory IV), the energy almost converged, and the radius was the smallest among the eigenstates except for the 0_1^+ and 0_2^+ states. The suppression of radius indicated the localization of the wave function, and it was suggested that this eigenstate was resonant. Furthermore, the 0_4^+ state had the second-strongest monopole transition to the ground state, as shown in Table IV. Regarding the 0_3^+ state (trajectory III), neither the radius nor the energy converged, but the radius of this state was smaller than the radius of the higher states (fourth to seventh), and in particular, the strength of the monopole transition to 0_2^+ was high. The large value of the monopole transition to 0_2^+ is the feature of the breathing mode of the Hoyle state reported in Refs. [19,21]. The analysis in the next section indicates that the 0_3^+ state is the $2\hbar\omega$ excitation from the Hoyle state.

Figure 7 shows the contour maps of the squared overlap between the eigenfunctions and the OS-THSR wave function with variables B_1 and B_2 , which are extended to the independent parameters in Eq. (43). The case of $B_1 = B_2$ corresponds to the original THSR wave function, which is indicated by the dotted line in each panel. Within the range shown in the figure, no significant amount of overlap was found except for the 0_1^+ , 0_2^+ , 0_3^+ , and 0_4^+ states assigned here. The detailed analysis is described in the next section.

IV. DISCUSSION

First, we compared our results with other theoretical calculations and experimental data for the four low-lying 0^+ states (Fig. 8). The results labeled “THSR1,” “THSR2,” and “BB (REM)” were taken from Refs. [21], [19,36], and [37], respectively. These calculations were performed using the Volkov No. 2 force [24] with the Majorana parameter $M = 0.59$, whose strength parameters were slightly modified [2]. In the GCM calculations of “THSR1” and “THSR2,” the extended and deformed THSR wave functions were used as the basis wave functions. In the GCM calculation of “BB (REM),” the BB wave functions were used, and the selection of basis wave functions was performed via the real-time evolution method (REM). In all these calculations, the basis wave functions were chosen to satisfy the condition that the root-mean-square radii did not exceed a certain value to prevent the mixing of continuous states: 6 fm in “THSR1” and “THSR2” and 6.4 fm in “BB(REM).”

The ground state (0_1^+) obtained in the present calculation was more deeply bound and more compact than those of the experiment and other calculations using the Volkov force. These results are a characteristic of the AV4P potential not exhibiting saturation with respect to the density [35]. However, despite using the AV4P potential with a strong repulsive core, the Hoyle state (0_2^+) was obtained slightly above the threshold energy, as obtained from the other calculations using the Volkov force. The strong repulsive core is expected to hardly act between the clusters when the system is diluted. The density of the Hoyle state estimated from the radius is $1/4$ times that of the ground state.

To evaluate the effect of a strong repulsive core between clusters more precisely, we defined the strength of the short-range correlation between two α clusters using the correlated

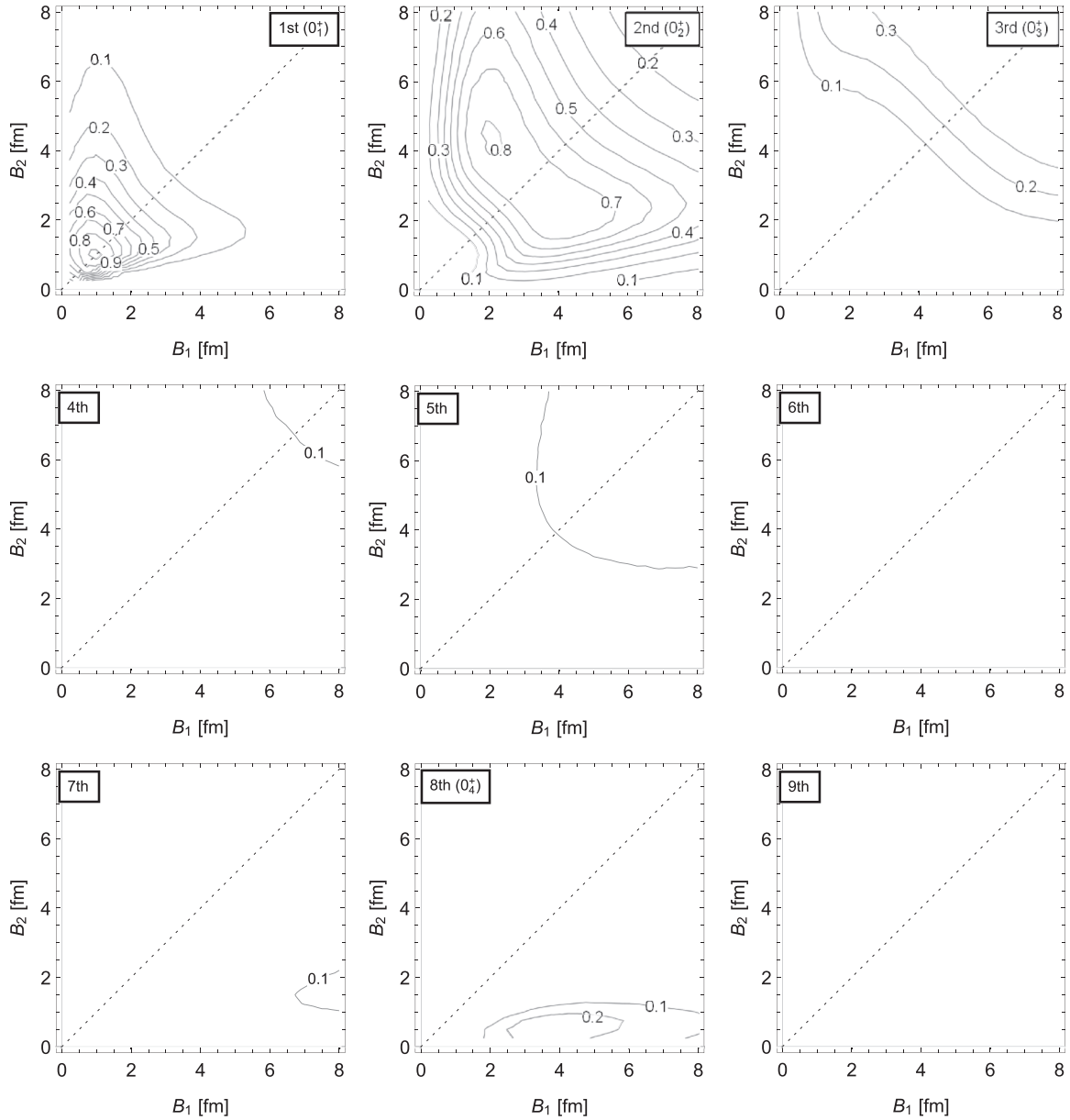


FIG. 7. Contour maps of the squared overlap with the $0S$ -THSR wave function for eigenfunctions of the nine lowest eigenstates of ^{12}C , corresponding to Table IV.

two-body kinetic-energy term in Eq. (10) as follows:

$$\langle \tilde{T}_2 \rangle_{\text{pair}} = \frac{\langle \tilde{T}_2 \rangle_{n\alpha} - n \langle \tilde{T}_2 \rangle_{\alpha}}{nC_2}, \quad (46)$$

which arises only from the short-range correlations in the UCOM procedure. Table V presents $\langle \tilde{T}_2 \rangle_{\text{pair}}$ normalized by $\langle \tilde{T}_2 \rangle_{\alpha}$ for the four 0^+ states. The effect of strong repulsion between two α clusters in the excited states is 3–7 times weaker than that in the ground state and $\leq 10\%$ of the effect within an α cluster. Therefore, the short-range strong repulsive core hardly affects correlations among constituent α clusters in the low-lying cluster-like excited states. This is the physical reason why similar results are obtained if the adopted NN potential appropriately represents the cluster-like property with and without a strong repulsive core.

The radii of the 0_3^+ and 0_4^+ states assigned here are significantly larger than those obtained via other calculations. This trend does not depend on the choice of interaction but depends on the selection of basis wave functions of the GCM calculation. In the other calculations, the basis wave functions were chosen to satisfy the condition that root-mean-square radii did

TABLE V. Strength of short-range correlations between two α clusters evaluated via Eq. (46) for four 0^+ states of ^{12}C , normalized by $\langle \tilde{T}_2 \rangle_{\alpha}$.

	0_1^+	0_2^+	0_3^+	0_4^+
$\frac{\langle \tilde{T}_2 \rangle_{\text{pair}}}{\langle \tilde{T}_2 \rangle_{\alpha}}$	0.298	0.093	0.042	0.060

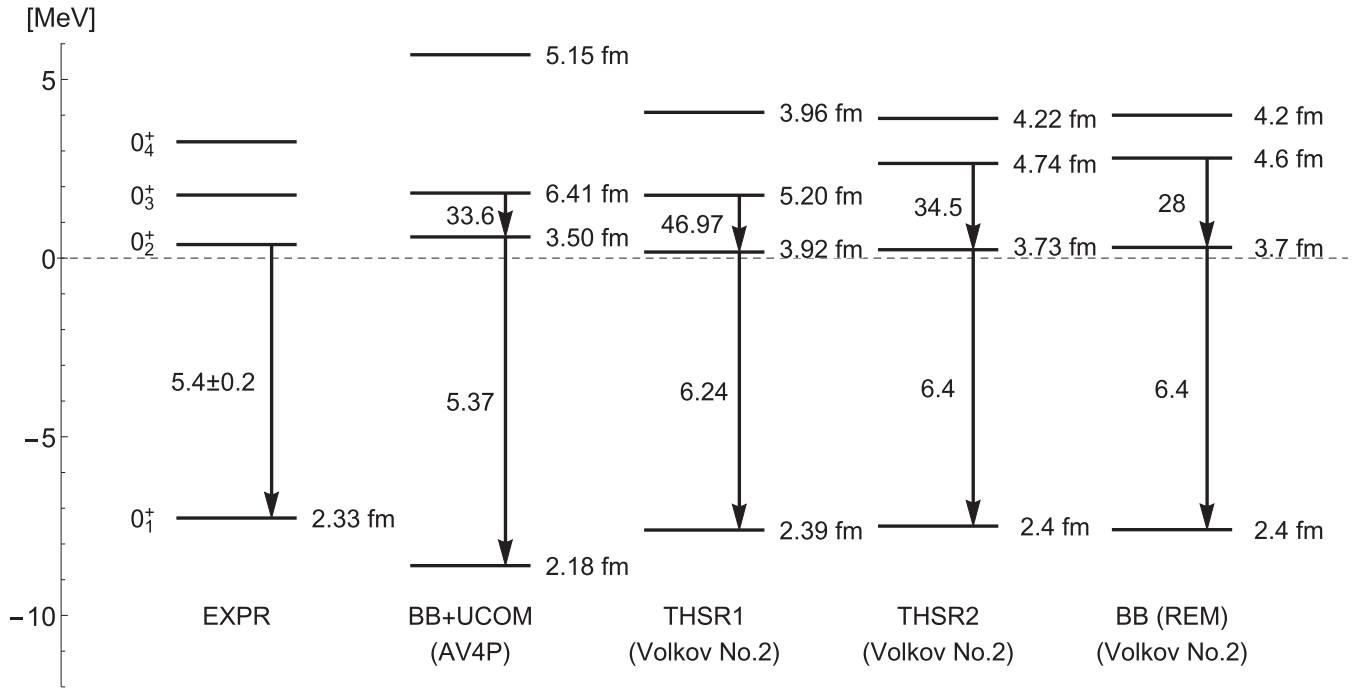


FIG. 8. Energy levels for four 0^+ states of ^{12}C in the present calculation (BB + UCOM) compared with the experimental data and other theoretical results. The energies were measured from the 3α threshold energy. The results labeled “THSR1,” “THSR2,” and “BB (REM)” were taken from Refs. [21], [19,36], and [37], respectively. The values shown to the right of the energy levels indicate the root-mean-square radii, and the values next to the arrows connecting two levels indicate the values of the matrix elements of a monopole transition between the connected states with units of $e\text{ fm}^2$. The experimental value of the charge radius for the ground state was converted into the point-proton radius.

not exceed a certain value, and the radii of the eigenstates were automatically suppressed. In this study, the radius was not restricted, but the range of the generator coordinates was restricted from $(\vec{R}_1, \vec{R}_2) = (1\text{ fm}, 1\text{ fm})$ to $(\vec{R}_1, \vec{R}_2) = (16\text{ fm}, 16\text{ fm})$. In addition, the radius of the 0_4^+ state was smaller than that of the 0_3^+ state in all the calculations.

In the study of the excited states in Hermitian quantum mechanics, preventing the mixing of continuous states is a difficult problem, and this mixing was particularly evident in the 0_3^+ state results. In all the calculations, the differences in the values of the energy, radius, and matrix element of the monopole transition between the 0_2^+ and 0_3^+ states were significant. In particular, although “THSR1” and “THSR2” used the same interaction and radius constraint, their values differed significantly. This indicates that the 0_3^+ state is extremely sensitive to the choice of the basis wave function and requires a non-Hermitian quantum-mechanical treatment, such as the complex-scaling method, for accurate discussion [18,38]. However, all the calculations indicated a large transition matrix element between the 0_2^+ and 0_3^+ states, and the three previous studies concluded that the 0_3^+ state was the breathing mode of the Hoyle state (0_2^+). It was directly shown in the present study that the 0_3^+ state is the vibrationally excited state from the Hoyle state, as discussed later.

The 0_4^+ state was obtained at a higher excitation energy compared with other calculations, but this was due to not differences in interactions but differences in variational wave

functions; that is, in the present calculations, the $^8\text{Be} + \alpha$ channel included only the $^8\text{Be}(0^+)$ state. Experiments have indicated that the 0_4^+ state has a large branching ratio to the $^8\text{Be}(2^+) + \alpha(D\text{-wave})$ channel [17]. Therefore, including the $^8\text{Be}(2^+) + \alpha$ channel in our calculations is a future issue, which is expected to reduce the energy of the 0_4^+ state.

We next analyzed the wave functions of the four 0^+ states through a comparison with THSR wave functions and examined the spatial feature of the four states from the view point of the α condensation.

The ground state is almost described by a single OS-THSR wave function with $(B_1, B_2) = (1.0\text{ fm}, 1.0\text{ fm})$, which has a squared overlap of 0.922 (upper left panel of Fig. 7). Because the OS-THSR wave function coincides with the shell-model Slater determinant as B_1 and B_2 go to zero, the ground state of ^{12}C is considered to have a shell-model-like structure because of the small values of B_1 and B_2 . In addition, the density estimated from its radius is 2.63 times that of the ground state of $^8\text{Be}(0_1^+)$.

The Hoyle state is 81.1% described by a single OS-THSR wave function with $(B_1, B_2) = (2.1\text{ fm}, 4.5\text{ fm})$ (upper middle panel of Fig. 7). In contrast to the ground state, the Hoyle state has a maximum squared overlap at large B_1 and B_2 values and the density estimated from its radius is low; that is, 0.636 times that of the ground state of ^8Be . Accordingly, the Hoyle state is considered an α -condensed state in which three α particles move almost freely in a self-consistent mean field. The value of B_1 was similar to that of the ground state of ^8Be ,

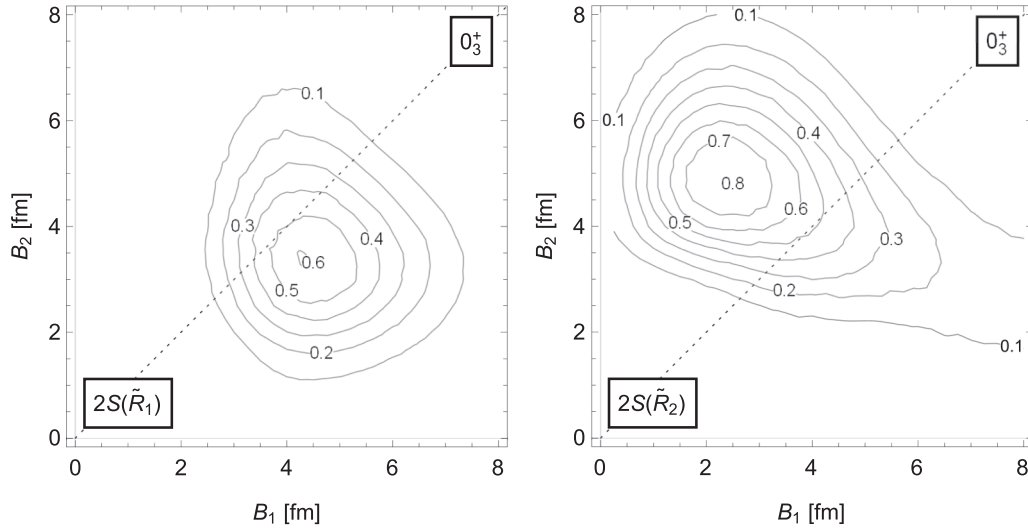


FIG. 9. Contour maps of the squared overlaps of the 0_3^+ state of ^{12}C with the $2S$ -THSR wave function with respect to R_1 (left panel) and R_2 (right panel).

and the value of B_2 was significantly larger than that of B_1 . These results indicate that the third α particle spreads over a wide range around the $^8\text{Be}(0_1^+)$ core occupying the $0S$ orbit.

The 0_3^+ and 0_4^+ states do not have a large overlap with a single $0S$ -THSR wave function (upper right and lower middle panels of Fig. 7), but the maximum overlap of the 0_4^+ state is located near the horizontal axis, and the points on $B_2 = 0$ fm describe the linear-chain structure with the aligned 3α particles because the third α cluster is fixed at the center-of-mass position of ^8Be when $B_2 = 0$. As shown later, such a structure is also observed in the contour map of the squared overlap with the $2S$ -THSR wave function with respect to \tilde{R}_2 .

Figure 9 shows the contour maps of the squared overlaps of the 0_3^+ state with the $2S$ -THSR wave function with respect to \tilde{R}_1 (left panel) and \tilde{R}_2 (right panel). The 0_3^+ state is 81.8%

described by a single $2S$ -THSR wave function with respect to the excitation of the α - 2α relative motion (\tilde{R}_2) with $(B_1, B_2) = (2.3 \text{ fm}, 4.9 \text{ fm})$. The value of B_1 is close to that of the ground state of ^8Be such that 0_3^+ has a structure in which the third α particle moves widely around the ^8Be core occupying the $2S$ orbit. This result is consistent with an experiment in which the 0_3^+ state decayed predominantly through the $^8\text{Be}(0^+) + \alpha(S\text{-wave})$ channel [17]. Furthermore, the position of the maximum point is almost the same as that of the Hoyle state (upper middle panel of Fig. 7). Accordingly, we conclude that the 0_3^+ state is a vibrational mode of α condensation from the Hoyle state, resulting in a large monopole transition matrix element between the 0_2^+ and 0_3^+ states.

Figure 10 presents the contour maps of the squared overlaps of the 0_4^+ state with the $2S$ -THSR wave function with

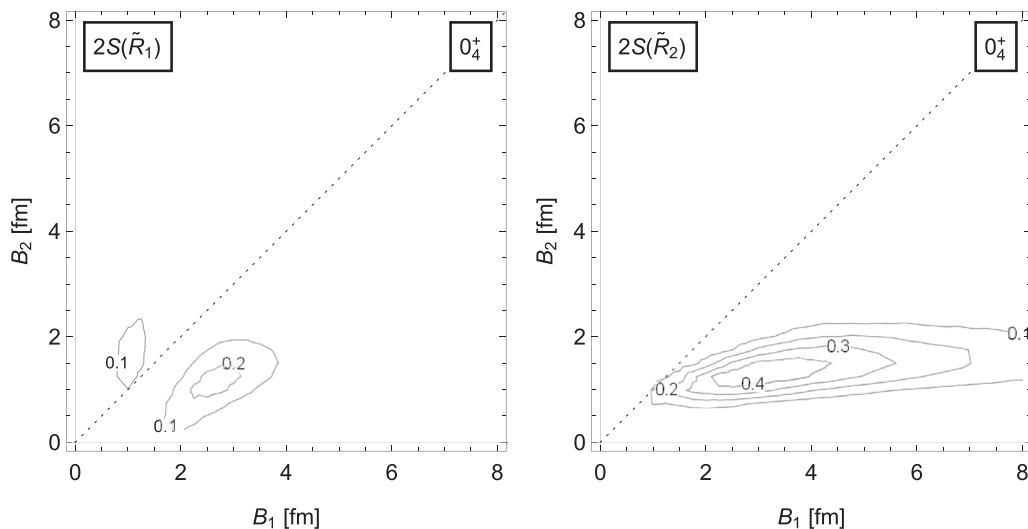


FIG. 10. Contour maps of squared overlaps of the 0_4^+ state of ^{12}C with the $2S$ -THSR wave function with respect to R_1 (left panel) and R_2 (right panel).

TABLE VI. Maximum squared overlaps between the eigenfunctions of the four 0^+ states of ^{12}C and the THSR wave function. In the present calculation (BB + UCOM), overlaps were evaluated for the single $0S$ - and $2S$ -THSR wave functions. In the “THSR1” and “THSR2” calculations, overlaps were evaluated for the single extended and deformed THSR wave functions projected to 0^+ and for them when the orthogonality to the single THSR wave functions giving the maximum overlap with the states below the state of interest. More information can be found in Refs. [20,21].

	BB + UCOM (AV4P)		THSR1 (Volkov No. 2)		THSR2 (Volkov No. 2)	
	0S-THSR w.f.	2S-THSR w.f.	Deformed THSR w.f. projected to 0^+			
	Single w.f.	$[2\alpha\text{-}\alpha(2S\text{-wave})]$ Single w.f.	Single w.f.	Orthogonalized w.f.	Single w.f.	Orthogonalized w.f.
0_1^+	0.922	–	0.978		0.978	
0_2^+	0.811	–	0.837	0.983	0.79	0.992
0_3^+	0.396	0.818	0.290	0.944	0.19	0.89
0_4^+	0.272	0.501	0.446	–	0.47	0.81

respect to \tilde{R}_1 (left panel) and \tilde{R}_2 (right panel). The 0_4^+ state was 50.1% described by a single $2S$ -THSR wave function with respect to \tilde{R}_2 with $(B_1, B_2) = (3.1 \text{ fm}, 1.3 \text{ fm})$. Because the maximum position is slightly away from the horizontal axis on which the structure indicates a linear chain, the intrinsic state of 0_4^+ is considered to have a bent-arm structure, as indicated by lattice CEFT [6], no-core MCSM [7], AMD [22] and FMD [23] calculations. As noted previously, the 0_4^+ state mainly decays through the $^8\text{Be}(2^+) + \alpha(D\text{-wave})$ channel [17]; therefore, it is necessary to consider the $^8\text{Be}(2^+) + \alpha$ channel for further investigation.

Table VI presents the maximum values of the squared overlaps between the eigenfunctions of the four 0^+ states and the THSR wave functions. The present calculations are compared with the “THSR1” and “THSR2” calculations. Approximately 80% of the eigenfunction of the Hoyle state (0_2^+) was described by the single THSR wave function in both the present calculation (the spherical $0S$ -THSR wave function) and the “THSR1” and “THSR2” calculations (the deformed THSR wave function projected to the 0^+ state). Furthermore, when the orthogonality to the single THSR wave function giving the maximum overlap with the eigenfunction of the ground state (0_1^+) was imposed, the maximum value of squared overlap exceeds 0.9. In the present calculation, the maximum value imposing the orthogonality was 0.944 at $(B_1, B_2) = (1.7 \text{ fm}, 4.0 \text{ fm})$.

For the 0_3^+ state, almost 40% of its eigenfunction was described by the single $0S$ -THSR wave function in the present calculation, whereas only 20%–30% was represented by the single deformed THSR wave function in the “THSR1” and “THSR2” calculations. When the orthogonality to the single THSR wave function giving the maximum overlap with the eigenfunctions of the 0_1^+ and 0_2^+ states was imposed, the maximum value of the squared overlap became 0.90–0.95 in the “THSR1” and “THSR2” calculations. In the present calculation, approximately 80% of the 0_3^+ state was described by the single $2S$ -THSR wave function. Therefore, it is suggested that the main component of the 0_3^+ states is the $^8\text{Be} + \alpha$ ($2S$ -wave) configuration. A detailed analysis of the 0_4^+ state considering the $^8\text{Be}(2^+) + \alpha$ channel will be performed in a future study.

Finally, we verified the possibility of an α -condensed state of $2D$ -wave excitation in $^8\text{Be}(2^+)$. The GCM calculation was performed for 2^+ states of ^8Be in the same manner as that for 0^+ states of ^8Be . Figure 11 shows the trajectories of the resulting eigenstates in the $(\langle r^2 \rangle)^{1/2} - E'$ plane. It was found that the state with the smallest radius in each GCM calculation (red points) existed around $E' = 3.08 \text{ MeV}$ where the trajectories were bent (dotted line). Such a suppression of radius was also seen in trajectory IV (0_4^+) of ^{12}C (Fig. 6) due to the localization of the resonant state, and it is suggested that there is a resonance state around $E_x = 3.3 \text{ MeV}$, which was consistent with the GFMC result indicating that the 2_1^+ state of ^8Be was at $E_x = 3.1 \text{ MeV}$ [28].

Figure 12 shows the squared overlap between eigenfunctions at the bending point ($E' = 3.08 \text{ MeV}$) and $2D$ -THSR wave function describing an α -condensed state with the relative motion excited to $2D_0$ wave. The maximum overlap occurred at $B = 1.7 \text{ fm}$. As the number of generator coordinates increased, the peak height gradually decreased, but

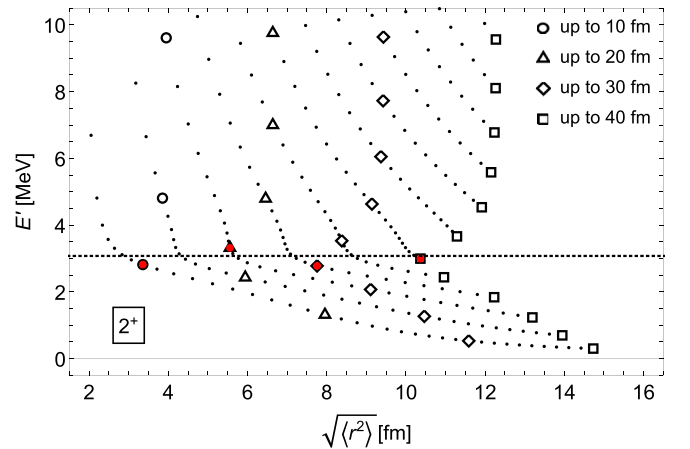


FIG. 11. Trajectories of eigenstates of $^8\text{Be}(2^+)$ in the $(\langle r^2 \rangle)^{1/2} - E'$ ($=E - 2E_\alpha$) plane. Circles, triangles, diamonds, and squares indicate the calculations up to 10, 20, 30, and 40 fm, respectively. Red points indicate the eigenstate with the minimum root-mean-square radius in each GCM calculation.

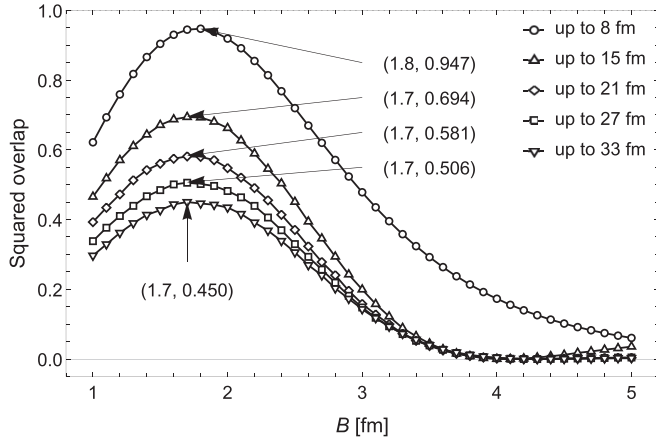


FIG. 12. Squared overlaps between the eigenstate of ${}^8\text{Be}(2^+)$ at $E - E_{2\alpha} = 3.08$ MeV and the $2D$ -THSR wave function describing an α -condensed state with the relative motion excited to $2D_0$ wave. Circles, triangles, diamonds, squares, and inverted triangles indicate the GCM calculations up to 8, 15, 21, 27, and 33 fm, respectively.

the reduction rate of the peak height gradually decreased. Such behavior is caused by the mixing of continuous states, and, therefore, it is suggested that ${}^8\text{Be}(2_1^+)$ contains an α -condensed state that is excited from the $0S$ wave to the $2D$ wave. How such a state affects the α -condensed states of ${}^{12}\text{C}$ is of interest.

V. CONCLUSIONS

We investigated the low-lying 0^+ states of ${}^{12}\text{C}$ in a 3α cluster model (BB wave function) using the AV4P potential, which has a strong repulsive core. We confirmed four experimentally observed 0^+ states that were also indicated by calculations using the Volkov No. 2 force. The AV4P potential does not exhibit saturation, and the ground state is deeply bound; however, the energy spectrum near the threshold is almost identical to that obtained with the Volkov No. 2 force, which is a phenomenological potential and has no short-range repulsion. This is because 0^+ states near the threshold are cluster-like states and have diluted structures, and short-range repulsion seldom acts between the constituent clusters.

The properties of the four 0^+ states, such as the radius and monopole transition matrix elements, exhibited similar tendencies to those obtained in previous studies. In particular, the matrix element of the monopole transition between the 0_2^+ and 0_3^+ states was large, indicating that the 0_3^+ state was the breathing mode of the Hoyle state, as in previous studies. From the analysis of the overlaps with the ordinal $0S$ -THSR wave function and the $2S$ -THSR wave function defined in this study, it is shown more specifically that the 0_3^+ state is a vibrationally excited state of the Hoyle state; that is, from the ${}^8\text{Be}(0_1^+) + \alpha(0S\text{-wave})$ state to the ${}^8\text{Be}(0_1^+) + \alpha(2S\text{-wave})$ state. The eigenfunctions of the 0_2^+ and 0_3^+ states obtained in the GCM calculation can be $\geq 80\%$ described by single $0S$ -THSR and $2S$ -THSR wave functions, and the condensation radii where the overlaps are maximum in the 0_2^+ and 0_3^+ states are almost the same. However, the eigenfunction of the 0_3^+ state is sensitive to the choice of basis wave functions owing to the contamination of continuous states, and it requires detailed studies that accurately describe resonant states, such as the complex scaling method.

The 0_4^+ state was obtained at a higher excited energy compared with the THSR and BB(REM) calculations. This is because the ${}^8\text{Be}(2^+) + \alpha$ channel in the 0_4^+ state, which is important as shown both experimentally and theoretically, was not included in the present study. However, despite the absence of the ${}^8\text{Be}(2^+) + \alpha(S\text{-wave})$ channel, it was observed that the 0_4^+ state exhibits a bent-arm structure, as observed in the previous studies. Calculations involving the ${}^8\text{Be}(2^+) + \alpha$ channel are necessary for a detailed discussion. As the possibility that the ${}^8\text{Be}(2_1^+)$ state is an α -condensed state with $2D$ wave was illustrated in this study, it is of interest to determine how this condensed state relates to low-lying cluster excited states in ${}^{12}\text{C}$ —not only four 0^+ states but also the 2_2^+ state, which has been demonstrated to be related to the Hoyle state. This will be discussed in our forthcoming reports.

ACKNOWLEDGMENTS

This work was partly achieved using Supercomputer for Quest to Unsolved Interdisciplinary Datascience (SQUID) at the Cybermedia Center, Osaka University. One of the authors (H. Takemoto) acknowledges that part of this work was motivated by Prof. P. Schuck and is grateful to Prof. A. Tohsaki for the fruitful discussions.

- [1] K. Ikeda, N. Takigawa, and H. Horiuchi, *Prog. Theor. Phys. Suppl.* **E68**, 464 (1968).
- [2] Y. Fujiwara, H. Horiuchi, K. Ikeda, M. Kamimura, K. Katō, Y. Suzuki, and U. Uegaki, *Prog. Theor. Phys. Suppl.* **68**, 29 (1980).
- [3] F. Hoyle, *Astrophys. J., Suppl. Ser.* **1**, 121 (1954).
- [4] R. B. Wiringa, S. C. Pieper, J. Carlson, and V. R. Pandharipande, *Phys. Rev. C* **62**, 014001 (2000).
- [5] J. Carlson, S. Gandolfi, F. Pederiva, S. C. Pieper, R. Schiavilla, K. E. Schmidt, and R. B. Wiringa, *Rev. Mod. Phys.* **87**, 1067 (2015).
- [6] E. Epelbaum, H. Krebs, T. A. Lähde, D. Lee, and Ulf-G. Meißner, *Phys. Rev. Lett.* **109**, 252501 (2012).
- [7] T. Otsuka, T. Abe, T. Yoshida, N. Shimizu, N. Itagaki, Y. Utsuno, J. Vary, P. Maris, and H. Ueno, *Nat. Commun.* **13**, 2234 (2022).
- [8] H. Horiuchi, *Prog. Theor. Phys.* **51**, 1266 (1974).
- [9] H. Horiuchi, *Prog. Theor. Phys.* **53**, 447 (1975).
- [10] E. Uegaki, S. Okabe, Y. Abe, and H. Tanaka, *Prog. Theor. Phys.* **57**, 1262 (1977).
- [11] E. Uegaki, Y. Abe, S. Okabe, and H. Tanaka, *Prog. Theor. Phys.* **59**, 1031 (1978).

- [12] E. Uegaki, Y. Abe, S. Okabe, and H. Tanaka, *Prog. Theor. Phys.* **62**, 1621 (1979).
- [13] M. Kamimura, *Nucl. Phys. A* **351**, 456 (1981).
- [14] A. Tohsaki, H. Horiuchi, P. Schuck, and G. Röpke, *Phys. Rev. Lett.* **87**, 192501 (2001).
- [15] B. Zhou, Y. Funaki, H. Horiuchi, and A. Tohsaki, *Front. Phys.* **15**, 14401 (2020).
- [16] M. Itoh, H. Akimune, M. Fujiwara, U. Garg, N. Hashimoto, T. Kawabata, K. Kawase, S. Kishi, T. Murakami, K. Nakanishi, Y. Nakatsugawa, B. K. Nayak, S. Okumura, H. Sakaguchi, H. Takeda, S. Terashima, M. Uchida, Y. Yasuda, M. Yosoi, and J. Zenihiro, *Phys. Rev. C* **84**, 054308 (2011).
- [17] M. Itoh, H. Akimune, M. Fujiwara, U. Garg, T. Kawabata, K. Kawase, T. Murakami, K. Nakanishi, Y. Nakatsugawa, H. Sakaguchi, S. Terashima, M. Uchida, Y. Yasuda, M. Yosoi, and J. Zenihiro, *J. Phys.: Conf. Ser.* **436**, 012006 (2013).
- [18] C. Kurokawa and K. Katō, *Phys. Rev. C* **71**, 021301(R) (2005).
- [19] Y. Funaki, *Phys. Rev. C* **92**, 021302(R) (2015).
- [20] Y. Funaki, *Phys. Rev. C* **94**, 024344 (2016).
- [21] B. Zhou, A. Tohsaki, H. Horiuchi, and Z. Ren, *Phys. Rev. C* **94**, 044319 (2016).
- [22] Y. Kanada-En'yo, *Prog. Theor. Phys.* **117**, 655 (2007).
- [23] M. Chernykh, H. Feldmeier, T. Neff, P. vonNeumann-Cosel, and A. Richter, *Phys. Rev. Lett.* **98**, 032501 (2007).
- [24] A. B. Volkov, *Nucl. Phys.* **74**, 33 (1965).
- [25] R. B. Wiringa, V. G. J. Stoks, and R. Schiavilla, *Phys. Rev. C* **51**, 38 (1995).
- [26] R. Machleidt, *Phys. Rev. C* **63**, 024001 (2001).
- [27] V. G. J. Stoks, R. A. M. Klomp, C. P. F. Terheggen, and J. J. de Swart, *Phys. Rev. C* **49**, 2950 (1994).
- [28] R. B. Wiringa and S. C. Pieper, *Phys. Rev. Lett.* **89**, 182501 (2002).
- [29] H. Feldmeier, T. Neff, R. Roth, and J. Schnack, *Nucl. Phys. A* **632**, 61 (1998).
- [30] R. Roth, T. Neff, H. Hergert, and H. Feldmeier, *Nucl. Phys. A* **745**, 3 (2004).
- [31] T. Myo, H. Toki, and K. Ikeda, *Prog. Theor. Phys.* **121**, 511 (2009).
- [32] Q. Zhao, M. Isaka, T. Myo, M. Lyu, H. Toki, H. Horiuchi, H. Takemoto, and N. Wan, *Prog. Theor. Exp. Phys.* **2021**, 063D02 (2021).
- [33] D. M. Brink, in *Proceeding of the International School of Physics "Enrico Fermi" Course XXXVI, Varenna on Lake Como, Villa Monsaxteror* (Academic Press, 1965), pp. 247–276.
- [34] T. Neff and H. Feldmeier, *Nucl. Phys. A* **713**, 311 (2003).
- [35] T. Myo, H. Takemoto, M. Lyu, N. Wan, C. Xu, H. Toki, H. Horiuchi, T. Yamada, and K. Ikeda, *Phys. Rev. C* **99**, 024312 (2019).
- [36] B. Zhou, Y. Funaki, A. Tohsaki, H. Horiuchi, and Z. Ren, *Prog. Theor. Exp. Phys.* **2014**101D01 (2014).
- [37] R. Imai, T. Tada, and M. Kimura, *Phys. Rev. C* **99**, 064327 (2019).
- [38] T. Myo, Y. Kikuchi, H. Masui, and K. Kato, *Prog. Part. Nucl. Phys.* **79**, 1 (2014).